Mapping oil spills on sea water using spectral mixture analysis of hyperspectral image data

Javier Plaza*, Rosa Pérez, Antonio Plaza, Pablo Martínez and David Valencia
Neural Networks and Signal Processing Group (GRNPS), Computer Science Department,
University of Extremadura, Avda. de la Universidad S/N, 10071 Cáceres, SPAIN.

ABSTRACT

During the last years, several terrestrial ecosystems have suffered from large spill oil events threatening coastal habitats and species. Some recent examples include the 2002 Prestige tanker oil spill in Galicia, Northern Spain, as well as repeated oil spill leaks evidenced in the Santa Barbara coastline in California, and the Patuxent river (Chesapeake watershed) in Maryland. Both spaceborne and airborne hyperspectral sensors allow detailed identification of materials, and very accurate (sub-pixel) estimates of their fractional abundance covers. In the event of an oil spill, the information produced by remotely sensed hyperspectral instruments can be used to design an effective environmental oil spill protection and response plan, which could help to reduce the environmental consequences of the spill and cleanup efforts, as well as to protect human life. In this paper, we discuss a novel automated hyperspectral target detection technique for determining the level of oil contamination of polluted areas in the shoreline. The method is based on the simultaneous use of spatial and spectral information by extended mathematical morphology operations. Both simulated and real hyperspectral data, collected over polluted areas, are used in this work to illustrate the effectiveness of the proposed approach.

Keywords: Standoff detection, Oil spill detection and mapping, Hyperspectral imagery, Morphological analysis.

1. INTRODUCTION

Large spills of oil and related petroleum products in the marine environment can have serious biological and economic impacts[1]. Public and media scrutiny is usually intense following a spill, with demands that the location and extent of the oil spill be identified. Hyperspectral remote sensing is playing an increasingly important role in oil spill response efforts[2,3,4]. Recent improvements in sensor technology, space power, computers, pattern recognition algorithms, and communication systems suggest that efficient standoff detection and identification systems are feasible[5]. These systems involve passive and active methods for sensing of chemical and biological materials when the sensor is physically separated from the site of interest. Nearly any chemical or biological element can be a pollutant, meaning that in large enough quantities it has the potential for causing ecological damage. In the event of an oil spill on sea water, fast and accurate determination of hazard areas is needed, particularly if monitoring large quantities of oil spilled.

During the last years, several terrestrial ecosystems have suffered from large spill oil events threatening coastal habitats and species. Some recent examples include the 2002 Prestige tanker oil spill in Galicia, Northern Spain[6] (see Fig. 1), as well as repeated oil spill leaks evidenced in the Santa Barbara coastline in California, and the Patuxent river (Chesapeake watershed) in Maryland. Chemical measurements of man's influences on coastal environments, such as those mentioned above, fall into three general classes: 1) the assessment of the major chemical constituents of sea water including salt, dissolved oxygen, major nutrients (nitrogen, phosphate, silicate) and carbon; 2) the quantification of trace elements, principally metals, in the water, the bottom, and the sea life; and 3) the measurement of pollutant hydrocarbons including synthetic organics and petroleum hydrocarbons. The result of many such measurements is to determine where the nutrients and pollutants are in the ecosystem. In order to discover whether an area is polluted or otherwise influenced, its chemical and biological characteristics must be compared with some area that is as similar as possible but seems not to have been affected by man. These comparative sites are called reference or control stations[1]. Generally, it is sensible to have as many reference sites as possible so that a range of normal values is available for comparison.

* E-mail: aplaza@unex.es; Phone: +34 927257195; Fax: +34 927257203.

Chemical and Biological Standoff Detection III, edited by James O. Jensen, Jean-Marc Thériault,
Proc. of SPIE Vol. 5995, 599509, (2005) · 0277-786X/05/$15 · doi: 10.1117/12.631149

(a) (b) (c)

Figure 1. Prestige tanker 2002 shipwreck in Galicia, Northern Spain. (a) Tanker breaking and subsequent oil leakage on sea water. (b) Cleanup efforts at Galicia coastal environments. (c) Biological impacts of the Prestige environmental disaster (© Copyright La Voz de Galicia, S.A. Polígono de Sabón, Arteixo, A Coruña, Spain).

Airborne and space-borne hyperspectral sensors have been widely evaluated in terms of their usefulness in responding to oil spills[4]. These sensors allow detailed identification of materials, and very accurate (sub-pixel) estimates of their fractional abundance covers[7]. In the event of an oil spill, the information produced by remotely sensed hyperspectral instruments can be used to design an effective environmental oil spill protection and response plan, which could help to reduce the environmental consequences of the spill and cleanup efforts, as well as to protect human life. In this paper, we describe an innovative approach for standoff detection using hyperspectral data. The proposed approach, which is based on mathematical morphology concepts[8], is able to use both the spatial and spectral information contained in the data set to detect chemical and biological agents. Section 2 describes the proposed approach. Section 3 describes real multispectral data, collected by the CASI sensor right after the 2002 Prestige tanker oil spill in Galicia, northern Spain. These data, along with AVIRIS spectral signatures collected during an oil spill event in the Santa Barbara coastline in California, are used to illustrate the performance of the proposed method in Section 4. The paper concludes with some remarks in Section 5.

2. STANDOFF DETECTION BY EXTENDED MORPHOLOGICAL OPERATIONS

2.1. Extending mathematical morphology to multispectral imagery

Our attention in this section focuses primarily on the development of a mechanism to extend morphological operations to hyperspectral image data. The two basic operations of classic mathematical morphology are dilation and erosion[8]. Following a usual notation, let us consider a grayscale image f, defined on a space E. Typically, E is the 2-Dimensional (2-D) continuous space R^2 or the 2-D discrete space Z^2. In the following, we refer to morphological operations defined on the discrete space. The flat erosion of f by using a structuring element (SE) $B \subset Z^2$ is defined by

$$(f \otimes B)(x, y) = \bigwedge_{(s,t) \in Z^2(B)} f(x + s, y + t), (x, y) \in Z^2. \quad ..(1)$$

where $Z^2(B)$ denotes the set of discrete spatial coordinates associated to pixels lying within the neighborhood defined by B and $\bigwedge$ denotes the minimum. On the other hand, the flat dilation of f by B is defined by

$$(f \oplus B)(x, y) = \bigvee_{(s,t) \in Z^2(B)} f(x - s, y - t), (x, y) \in Z^2, \quad (2)$$

where $\bigvee$ denotes the maximum. In order to extend the two basic morphological operations to hyperspectral images[9], let us now consider an image $\boldsymbol{f}$, defined on the N-Dimensional (N-D) continuous space, where N is the number of spectral

channels. An ordering relation can be imposed in the set of pixels lying within a flat structuring element, denoted by B, by defining metrics that calculate the cumulative distance between one particular pixel $\boldsymbol{f}(x,y)$, where $\boldsymbol{f}(x,y)$ denotes an N-D vector at discrete spatial coordinates $(x,y)\in Z^2$, and every other pixel in the neighborhood given by B. Based on the previous considerations, flat extended dilation and flat extended erosion can be respectively defined as follows:

$$(\boldsymbol{f}\oplus B)(x,y)=\arg\left\{\bigwedge_{(s,t)\in Z^2(B)}\left[\sum_s\sum_t \mathbf{Dist}(\boldsymbol{f}(x,y),\boldsymbol{f}(x+s,y+t))\right]\right\} \tag{3}$$

$$(\boldsymbol{f}\otimes B)(x,y)=\arg\left\{\bigvee_{(s,t)\in Z^2(B)}\left[\sum_s\sum_t \mathbf{Dist}(\boldsymbol{f}(x,y),\boldsymbol{f}(x-s,y-t))\right]\right\} \tag{4}$$

where **Dist** is a point-wise distance measure between two N-D vectors. The choice of **Dist** is a key topic in the resulting ordering relation between hyperspectral image pixels within the structuring element. In this work, **Dist** refers to the spectral angle distance, which is invariant to unknown multiplicative scaling that may arise due to different illumination conditions and sensor observation angle. This choice allows us to use extended morphological operations for the purpose of pure signature (endmember) extraction[10].

2.2. Extended morphological profiles

Our main goal in this section is to incorporate the idea of multiscale analysis into extended morphological operations, so that the most appropriate SE size can be selected at each pixel by plotting the morphological operation output at each pixel against the value of the varying SE size[11]. The resulting plot is called a morphological profile[12]. Let us consider a hyperspectral image $\boldsymbol{f}$ defined on R^N. Given a flat SE (designed by B) of minimal size, extended opening by reconstruction can be defined by

$$(\boldsymbol{f}\circ B)^k(x,y)=\bigvee_{k\geq 1}\left[\delta_B^k(\boldsymbol{f}\circ B\,|\,\boldsymbol{f})\right](x,y), \tag{5}$$

where the elementary term $\left[\delta_B(\boldsymbol{f}\circ B\,|\,\boldsymbol{f})\right](x,y)$ is an extended geodesic dilation, defined as the maximum of the elementary dilation of $\boldsymbol{f}\circ B$ using B at pixel (x,y) and the value of $\boldsymbol{f}(x,y)$. This operation is repeated *k* times until idempotence is reached.

$$\left[\delta_B^k(\boldsymbol{f}\circ B\,|\,\boldsymbol{f})\right](x,y)=\left[\underbrace{\delta_B\delta_B\cdots\delta_B}_{k\ \text{times}}(\boldsymbol{f}\circ B\,|\,\boldsymbol{f})\right](x,y) \tag{6}$$

In a similar fashion, extended closing by reconstruction is given by

$$(\boldsymbol{f}\bullet B)^k(x,y)=\bigwedge_{k\geq 1}\left[\varepsilon_B^k(\boldsymbol{f}\bullet B\,|\,\boldsymbol{f})\right](x,y) \tag{7}$$

Extended morphological profiles are created as follows. Let the vector $\boldsymbol{p}_k^{\circ}(x,y)$ be the extended opening by reconstruction profile at the pixel (x,y) of the image $\boldsymbol{f}$, defined by:

$$\boldsymbol{p}_k^{\circ}(x,y)=\left\{(\boldsymbol{f}\circ B)^{\lambda}(x,y)\right\},\qquad \lambda=\{0,1,\ldots,k\}, \tag{8}$$

And let $\boldsymbol{p}_k^{\bullet}(x,y)$ be the extended closing by reconstruction profile at the pixel (x,y) of the image $\boldsymbol{f}$, defined by:

$$\boldsymbol{p}_k^{\bullet}(x,y)=\left\{(\boldsymbol{f}\bullet B)^{\lambda}(x,y)\right\},\qquad \lambda=\{0,1,\ldots,k\}, \tag{9}$$

Here $(\boldsymbol{f}\bullet B)^0(x,y)=\boldsymbol{f}(x,y)=(\boldsymbol{f}\circ B)^0(x,y)$ for $\lambda=0$. We define the derivative of the extended opening profile $\Delta\boldsymbol{p}_k^{\circ}(x,y)$ as the following vector, where $\lambda=\{1,2,\ldots,k\}$:

$$\Delta \boldsymbol{p}_k^{o}(x,y) = \left\{ \mathbf{Dist}\left[(\boldsymbol{f} \circ B)^{\lambda}(x,y), (\boldsymbol{f} \circ B)^{\lambda-1}(x,y) \right] \right\}. \quad (10)$$

By duality, the derivative of the closing profile $\Delta \boldsymbol{p}_k^{\bullet}(x,y)$ is defined as the vector:

$$\Delta \boldsymbol{p}_k^{\bullet}(x,y) = \left\{ \mathbf{Dist}\left[(\boldsymbol{f} \bullet B)^{\lambda}(x,y), (\boldsymbol{f} \bullet B)^{\lambda-1}(x,y) \right] \right\}. \quad (11)$$

Given all of the above, the multi-scale opening characteristic $\Phi_k^{o}(x,y)$ at the point (x,y) of the image $\boldsymbol{f}$ is defined as the SE size with the greatest associated value in $\Delta \boldsymbol{p}_k^{o}(x,y)$

$$\Phi_k^{o}(x,y) = \lambda \in \{1, 2, ..., k\}; \quad \mathbf{Dist}\left[(\boldsymbol{f} \circ B)^{\lambda}(x,y), (\boldsymbol{f} \circ B)^{\lambda-1}(x,y) \right] = \bigvee \Delta \boldsymbol{p}_k^{o}(x,y). \quad (12)$$

Similarly, the multi-scale closing characteristic $\Phi_k^{\bullet}(x,y)$ is defined as the SE size with the greatest associated value in the derivative of the extended closing profile $\Delta \boldsymbol{p}_k^{\bullet}(x,y)$

$$\Phi_k^{\bullet}(x,y) = \lambda \in \{1, 2, ..., k\}; \quad \mathbf{Dist}\left[(\boldsymbol{f} \bullet B)^{\lambda}(x,y), (\boldsymbol{f} \bullet B)^{\lambda-1}(x,y) \right] = \bigvee \Delta \boldsymbol{p}_k^{\bullet}(x,y). \quad (13)$$

2.3. Standoff detection algorithm

The proposed standoff detection algorithm, called ADMP (Automated Determination of Morphological Profiles), is summarized in Table 1. Firstly, those pixels that remain indifferent to the closing-by-reconstruction process but are replaced during opening by reconstruction can be designed as "pure". In contrast, those pixels that remain indifferent to the opening-by-reconstruction process but are replaced during closing by reconstruction can be labeled as "mixed". Hence, pure/mixed pixels can be easily identified by comparing the maximum derivative value obtained in the opening-by-reconstruction series, i.e. $\bigvee \Delta \boldsymbol{p}_k^{\bullet}(x,y)$, to the maximum derivative value produced by the closing-by-reconstruction series, i.e. $\bigvee \Delta \boldsymbol{p}_k^{o}(x,y)$. As shown in Table 1, if $\boldsymbol{f}(x,y)$ is labeled as "pure", then its associated purity index score $\Pi(x,y)$ is calculated as the residual between the extended opening-by-reconstruction and the original pixel. In contrast, if $\boldsymbol{f}(x,y)$ is designed as a mixed pixel by the algorithm, then $\Pi(x,y)$ is calculated as the residual between the extended closing-by-reconstruction image and the original pixel. In both cases, the operation is performed by using an optimum SE size, provided by $\Phi_k^{o}(x,y)$ and $\Phi_k^{\bullet}(x,y)$, respectively. A general block diagram of the proposed method is shown in Fig. 2.

Inputs:
  Hyperspectral pixel vector: $\boldsymbol{f}(x,y)$.
  Maximum number of iterations: k.
Outputs:
  Labeling of $\boldsymbol{f}(x,y)$ as "pure" or "mixed".
  Morphological profile purity index, $\Pi(x,y)$, for $\boldsymbol{f}(x,y)$.
Begin
  If $\bigvee \Delta \boldsymbol{p}_k^{o}(x,y) > \bigvee \Delta \boldsymbol{p}_k^{\bullet}(x,y)$ then
    Label $\boldsymbol{f}(x,y)$ as "pure".
      $\Pi(x,y) = \mathrm{Dist}\left[\boldsymbol{f}(x,y), (\boldsymbol{f} \circ B)^{\lambda^{o}}(x,y) \right]$, where $\lambda^{o} = \Phi_k^{o}(x,y)$.
  Else
    Label $\boldsymbol{f}(x,y)$ as "mixed".
      $\Pi(x,y) = \mathrm{Dist}\left[\boldsymbol{f}(x,y), (\boldsymbol{f} \bullet B)^{\lambda^{\bullet}}(x,y) \right]$, where $\lambda^{\bullet} = \Phi_k^{\bullet}(x,y)$.
End

Table 1. Pseudo-code of ADMP algorithm.

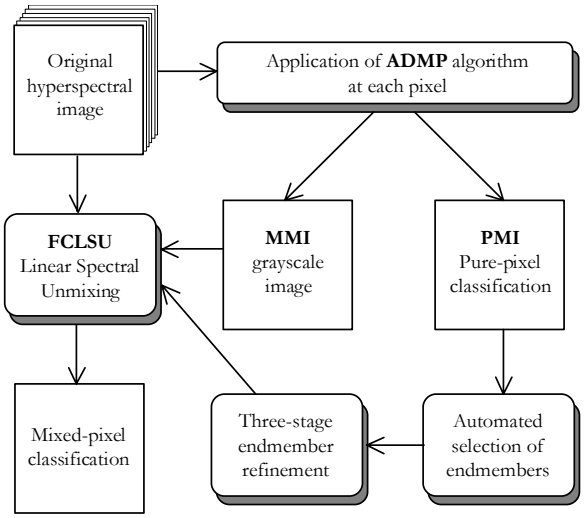

Figure 2. Block diagram of the proposed standoff detection technique.

As Fig. 2 shows, the input to the method is the full hyperspectral data cube, with no previous dimensionality reduction. Firstly, the ADMP algorithm is applied to each pixel of the original image. As a result, two grayscale images are produced, called pure morphological image (PMI) and mixed morphological image (MMI). The PMI contains those pixels labeled as "pure" by ADMP, while the MMI contains those pixels labeled as "mixed". Each pixel position (x, y) in both PMI and MMI stores the associated $\Pi(x, y)$ score calculated by ADMP. Automated endmember selection is performed at the PMI by using a threshold value. Several techniques have been discussed in the literature for automated thresholding of grayscale images. In our application, we have found appropriate results by using the multi-level Otsu method[13], an approach based on the minimization of the weighted sum of group variances. The final selection of endmembers is refined by a three-stage approach which consists of the following steps: 1) Spatial/spectral region growing, 2) Calculation of mean spectra from resulting regions, and 3) Redundant endmember thinning[9].

3. DATA

On November 13th, 2002, the Prestige oil tanker, loaded with 77 000 tons of heavy fuel oil, ran into trouble off Cap Finisterre, Galicia, Spain. An aerial survey undertaken by the Spanish authorities observed an oil leakage from the vessel, and on Tuesday, November 19th, 2002, the tanker split in two and sank. Much of the oil was spilled into the sea, but much remains on board and will continue to spill for several months. On Tuesday, December 3rd, 2002, the POLMAR plan (MARitime POLlution fight plan) was set up in France to face the pollution that arrives on the French coasts. In the following days and in order to help the POLMAR aircraft equipped with different kind of sensors, the French Navy Hydrographic and Oceanographic Service (SHOM) decided to test the feasibility of an airborne multispectral survey to detect and map the spill. An aerial remote sensing campaign was mobilized at short notice by AvelMor and Borstad Associates Ltd, using the Borstad Associates' Compact Airborne Spectrographic Imager (CASI) to obtain multispectral imagery over the spill off the coasts of Portugal and Spain[6].

Despite the adverse weather, imagery was acquired on December 16th, 18th, 19th and 20th. Some of the data were radiometrically calibrated, geometrically and geographically corrected in the evening of the flights to quickly obtain maps of the spill extent. The CASI was flown for this project in spatial mode and was configured to acquire 5 spectral channels (Table 1). The band configurations were chosen specifically for oil slicks mapping using spectral channels previously selected for similar oil slick mapping projects. Fig. 3 illustrates the spectral differences observed on the CASI images between sea water and oil on the surface. Hydrocarbons absorb incident energy in the ultraviolet portion of the electromagnetic spectrum (< 400 nm) and re-emit a part of it in the visible portion of the spectrum (400-650 nm) by a fluorescence phenomenon[14]. The reflected energy becomes more significant in the blue portion of spectrum. As shown in Fig. 3, in the visible region of the electromagnetic spectrum, oil has a higher surface reflectance than water, but also shows limited nonspecific absorption tendencies. Oil generally manifests throughout this visible spectrum. Overall,

however, oil has no specific characteristics that distinguish it from the background. The above physical properties allow the detection of hydrocarbons present on the ocean surface. From the spatial point of view, the detection is possible at a scale dependent on the spatial resolution of the sensor (slicks of approximately 5m² for this present experiment[6]).

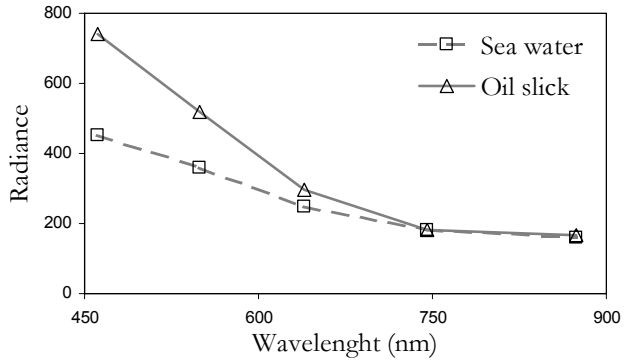

Figure 3. Spectral signatures of sea water and oil slick, collected right after the Prestige crisis using a CASI imaging spectrometer.

4. EXPERIMENTAL RESULTS

Before addressing our experimental results, it should be noted that ground-truth information related to the fractional coverage of materials inside each pixel is very difficult to obtain in a real-world standoff detection scenario[15]. As a result, mixed pixel analysis techniques are difficult to validate and substantiate[16]. In order to overcome the above limitation, a commonly accepted approach in the literature has been the use of simulated imagery. It should be taken into account that simulated scenes may not fully describe the complexity of a real scenario but, if carefully simulated, they have the advantage that the abundance fractions of constituents can be fully controlled and varied as necessary. In our experiments, the proposed method was tested on simulated scenes representing oil spill events. Spectral signatures from sea water and oil slick were selected from imagery collected right after two recent oil spill events:

1) Multispectral CASI data collected after the Prestige tanker oil spill event in Galicia, Northern Spain.
2) Hyperspectral AVIRIS data collected after an oil spill event in the Santa Barbara coastline in California.

The above spectral signatures were artificially mixed in computer simulations to create two simulated scenes, i.e. a multispectral scene made up of 5 spectral bands, and a hyperspectral scene with 224 spectral bands. Both scenes, with a size of 100x100 pixels, were simulated by using a simple linear mixture model with random non-negative abundance fractional values at each pixel. The sum of the two fractional abundances associated to the spectral constituents at each pixel, i.e. sea water and oil slick, adds to 1 (fully constrained linear mixture model[17]). Random noise was added to the two scenes above to simulate contributions from ambient (clutter) and instrumental sources. White gaussian noise was created by using numbers with a standard normal distribution obtained from a pseudorandom number generator and added to each pixel. For the simulations, we consider the SNR for each band as the ratio of the 50% signal level to the standard deviation of the noise[18]. This results in noise standard deviation that is roughly proportional to the average signal, a phenomenon often observed in radiometric data. Thus, the simulated hyperspectral data are created, based on a simple linear mixture model, by the following expression

$$\boldsymbol{s}(\mathrm{x},\mathrm{y}) = \left(\frac{\mathrm{SNR}}{2} + \boldsymbol{n}(\mathrm{x},\mathrm{y})\right) \cdot \sum_{\mathrm{j}=1}^{\mathrm{R}} \alpha_{\mathrm{j}}(\mathrm{x},\mathrm{y}) \cdot \boldsymbol{r}_{\mathrm{j}} \,, \tag{14}$$

where $\boldsymbol{s}(\mathrm{x},\mathrm{y})$ denotes a vector containing the simulated discrete spectrum at the pixel with spatial coordinates (x,y) of the simulated image, R is the total number of reference spectral signatures used to simulate the scene (2 in our case), $\alpha_{\mathrm{j}}(\mathrm{x},\mathrm{y})$ is the assigned fractional abundance of spectral signature $\boldsymbol{r}_{\mathrm{j}}$ at the pixel, and $\boldsymbol{n}(\mathrm{x},\mathrm{y})$ is the noise factor. An SNR value of 30:1 has been considered in the generation of each simulated scene. It should be noted that, for simplicity, multiple scattering effects have not been simulated. In addition, we have assumed uniform illumination throughout the scenes.

Prior to a full examination and discussion of results, it is important that the parameter values used for the proposed target detection technique. The spatial domain probed in this experiment by the ADMP algorithm was provided by a range of increasing square-shaped SE's with sizes ranging from 2x2 pixels (aprox. 10 meters) up to 7x7 pixels (aprox. 35 meters). This range was determined empirically after considerations on the relationship between spatial resolution of the data and minimum size of oil slicks[6]. After applying the ADMP algorithm, a set of endmembers associated with each constituent material of the simulated scenes (sea water and oil slick, respectively) was obtained. The abundance of each endmember was estimated by using fully constrained linear spectral unmixing[17]. We can visualize the performance of the proposed method on the two simulated scenes by plotting estimated in contrast to true abundances for the different constituents at each image pixel. In Fig. 4, scatterplots of true versus estimated abundance values and resulting root mean square error (RMSE) are shown for each material and scene. In general, we observe that acceptable quantitative agreements between the estimated and true abundances are obtained. However, we can notice that, when hyperspectral data are used, a significant improvement in terms of abundance estimation is obtained. Overall, the proposed method is able to accurately characterize mixed pixels made up of sea water and oil slick in different proportions, with sub-pixel precision. Nonetheless, it should be clarified that, because of the simple nature of the simulation carried out in this section, the above observations are not conclusive. In order to test these statements in a more complex situation, the development of further experiments using real data from oil spill events with reliable ground-truth are required.

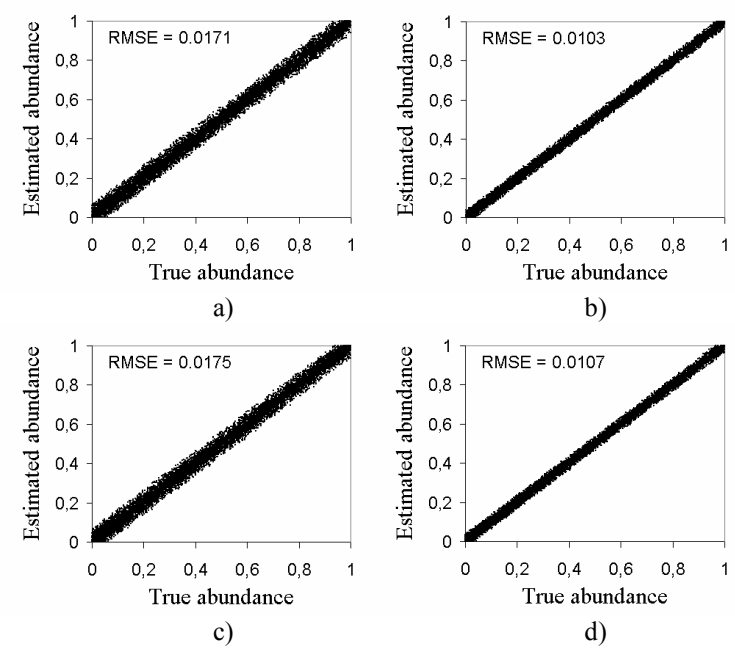

Figure 4. Scatterplots of true vs. estimated abundances for sea water in multi- (a) and hyperspectral (b) simulated data. Scatter-plots of true vs. estimated abundances for oil slick in multi- (c) and hyperspectral (d) simulated data.

CONCLUSIONS AND FUTURE LINES

We have described a novel approach to perform unsupervised standoff detection and mixed pixel classification in hyperspectral images. The proposed approach , based on the calculation of morphological profiles, can be successfully applied for the purpose of monitoring large oil spill events, and may help design effective environmental oil spill protection and response plans, which could help to reduce the environmental consequences of the spill and cleanup efforts. The method has a hierarchical effect that improves spatial localization for mapping applications. A drawback of the proposed approach concerns the necessity of looking at a range of increasing opening- and closing-by-reconstruction operations, which may result in a heavy computational burden when processing high-dimensional data. A research topic deserving future interest focuses on the development of effective implementation strategies. Massive parallel implementations using computer Beowulf-type low-cost cluster architectures are currently being tested in our laboratory in order to empower the proposed technique with real-time capabilities.

ACKNOWLEDGEMENT

We would like to thank The Military Oceanographic Center (CMO) from the Principal Establishment of the French Navy Hydrographic and Oceanographic Service (EPSHOM) for providing the CASI data collected right after the 2002 Prestige oil spill event in Galicia, Northern Spain. Support by Marc Lennon at SARL AvelMor, who helped us contact EPSHOM and provided very useful comments about CASI data, is gratefully acknowledged. We would also like to thank Robert O. Green, AVIRIS Experiment Scientist at NASA Jet Propulsion Laboratory, for his willingness to collaborate with us in this research topic, and for his advice on the usage of AVIRIS data collected after an oil spill event in Santa Barbara coastline, California.

REFERENCES

1. M.F. Fingas, and C.E. Brown, "Review of oil spill remote sensing," in *Proceedings of the Fifth International Conference on Remote Sensing for Marine and Coastal Environments*, Environmental Research Institute of Michigan, Ann Arbor, Michigan, pp. 211-218, 2000.
2. F. Salem, M. Kafatos, T. El-Ghazawi, R. Gomez, R. Yang, "Hyperspectral image analysis for oil spill detection," in *Summaries of NASA/JPL Airborne Earth Science Workshop*, Pasadena, CA, 2002.
3. F. Salem, M. Kafatos, "Hyperspectral image analysis for oil spill mitigation," in *22nd Asian Conference on Remote Sensing*, Singapore, 2001.
4. R. Bianchi, R.M. Cavalli, C.M. Marino, S. Pignatti, and M. Poscolieri, "Use of airborne hyperspectral images to assess the spatial distribution of oil spilled during the Trecate blow-out (Northern Italy)," in *Proc. SPIE*, vol. 2585, pp. 352-362, 1995.
5. C.-I Chang, *Hyperspectral imaging: spectral detection and classification*, Kluwer Academic Publishers, 2003.
6. M. Lennon, V. Mariette, A. Coat, V. Verbeque, P. Mouge, G.A. Borstad, P. Willis, R. Kerr, M. Alvarez, "Detection and mapping of the november 2002 Prestige tanker oil spill in Galicia, Spain, with the airborne multispectral CASI sensor," in *Proc. Third EARSeL Imaging Spectroscopy Workshop*, Herrsching, Germany, 2003.
7. R.O. Green et al., "Imaging spectroscopy and the airborne visible/infrared imaging spectrometer (AVIRIS)," *Remote Sensing of Environment*, vol. 65, pp. 227–248, 1998.
8. P. Soille, *Morphological analysis; Principles and applications*, Springer-Verlag, 2003.
9. A. Plaza, P. Martínez, R. Pérez, J. Plaza, "Spatial/spectral endmember extraction by multidimensional morphological operations," *IEEE Transactions on Geoscience and Remote Sensing*, vol. 40, pp. 2025-2041, 2002.
10. A. Plaza, P. Martínez, R. Pérez and J. Plaza, "A Quantitative and comparative analysis of endmember extraction algorithms from hyperspectral data," *IEEE Transactions on Geoscience and Remote Sensing*, vol. 42, no 2, pp.650-663, March 2004.
11. A. Plaza, P. Martínez, J. Plaza and R. Pérez, "Dimensionality reduction and classification of hyperspectral image data using sequences of extended morphological transformations," *IEEE Transactions on Geoscience and Remote Sensing*, vol. 43, no. 3, pp. 466-479, 2005.
12. M. Pesaresi, J.A. Benediktsson, "A new approach for the morphological segmentation of high resolution satellite imagery," *IEEE Transactions on Geoscience and Remote Sensing*, vol. 39, pp. 309-320, 2001.
13. N. Otsu, "A threshold selection method from gray-level histograms," IEEE *Transactions on Systems, Man, and Cybernetics*, vol. 9, pp. 62–66, 1979.
14. L. Balick, J.A. Di Benedetto, and S.S. Lutz, "A fluorescence emission spectral measurements for the detection of oil on shore," in *Proceedings of the Fourth Thematic Conference on Remote Sensing for Marine and Coastal Environments*, Environmental Research Institute of Michigan, Ann Arbor, Michigan, vol. 1, pp. 13-20, 1997.
15. C.-I Chang, S.-S Chiang, J. A. Smith, I. W. Ginsberg, "Linear spectral random mixture analysis for hyperspectral imagery," *IEEE Transactions on Geoscience and Remote Sensing*, vol. 40, no. 2, pp. 375-392, 2002.
16. C.-I Chang, H. Ren, "An experiment-based quantitative and comparative analysis of target detection and image classification algorithms for hyperspectral imagery". *IEEE Transactions on Geoscience and Remote Sensing*, vol. 38, no. 2, pp. 1044- 1063, 2000.
17. D. Heinz, C.-I Chang, "Fully constrained least squares linear mixture analysis for material quantification in hyperspectral Imagery," *IEEE Transactions on Geoscience and Remote Sensing*, vol. 39, pp. 529-545, 2000.
18. J. C. Harsanyi, C.-I Chang, "Hyperspectral image classification and dimensionality reduction: An orthogonal subspace projection approach," *IEEE Transactions on Geoscience and Remote Sensing*, vol. 32, no. 7, pp. 779-785, 1994.